

Non-Coplanar and Counter-Rotating Incommensurate Magnetic Order Stabilized by Kitaev Interactions in γ -Li₂IrO₃

A. Biffin¹, R. D. Johnson¹, I. Kimchi², R. Morris¹, A. Bombardi³, J. G. Analytis^{2,4}, A. Vishwanath^{2,4}, and R. Coldea¹

¹*Clarendon Laboratory, University of Oxford, Parks Road, Oxford OX1 3PU, U.K.*

²*Department of Physics, University of California, Berkeley, California 94720. USA.*

³*Diamond Light Source Ltd., Didcot OX11 0DE, U.K. and*

⁴*Materials Science Division, Lawrence Berkeley National Laboratory, Berkeley, California 94720. USA.*

Materials that realize Kitaev spin models with bond-dependent anisotropic interactions have long been searched for, as the resulting frustration effects are predicted to stabilize novel forms of magnetic order or quantum spin liquids. Here we explore the magnetism of γ -Li₂IrO₃, which has the topology of a 3D Kitaev lattice of inter-connected Ir honeycombs. Using resonant magnetic x-ray diffraction we find a complex, yet highly-symmetric incommensurate magnetic structure with non-coplanar and counter-rotating Ir moments. We propose a minimal Kitaev-Heisenberg Hamiltonian that naturally accounts for all key features of the observed magnetic structure. Our results provide strong evidence that γ -Li₂IrO₃ realizes a spin Hamiltonian with dominant Kitaev interactions.

PACS numbers: 75.25.-j, 75.10.Jm

Magnetic materials with bond-dependent anisotropic interactions are candidates to display novel forms of magnetic order or quantum spin liquid states, as exemplified by the Kitaev model on the honeycomb lattice [1]. Here all spins interact via nearest-neighbor Ising exchanges, but a different Ising axis (x, y, z) applies for the three different bonds emerging out of each lattice site. This leads to strong frustration effects that stabilize a novel gapless quantum spin liquid state with exotic excitations (Majorana fermions), which is exactly solvable in two dimensions. It was theoretically proposed [2] that such exotic Hamiltonians might be realized in magnetic materials containing edge-sharing cubic IrO₆ octahedra. The magnetic ground state of Ir⁴⁺ including the cubic crystal field and spin-orbit coupling is a complex spin-orbital doublet with $J_{\text{eff}} = 1/2$ [3], and super-exchange through the two 90° Ir-O-Ir paths is expected to lead to a dominant Ising interaction for the moment components normal to the Ir-O₂-Ir plane [2]. For a three-fold coordinated IrO₆ octahedron this leads to perpendicular Ising axes for the three nearest-neighbor bonds, as required for a Kitaev model. The 2D honeycomb-lattice α -Na₂IrO₃ [4–8] and α -Li₂IrO₃ [9, 10] are being intensively explored as candidate Kitaev materials, but as yet no clear evidence for novel Kitaev physics has been observed.

Generalizations of the Kitaev model to 3D lattices are also expected to have quantum spin liquid states [11–13]. The recently-synthesized structural polytypes “hyper-honeycomb” β -Li₂IrO₃ [14] and “harmonic” honeycomb γ -Li₂IrO₃ [15], which maintain the local three-fold coordination of edge-sharing IrO₆ octahedra, are prime candidates to display 3D Kitaev physics. To test for signatures of such physics we have performed resonant magnetic x-ray diffraction (RMXD) measurements [16] on single crystals of γ -Li₂IrO₃, scattering at the strong Ir L₃ resonance [5]. We have determined the complete magnetic structure for all 16 iridium sites in the unit cell, and

found an unexpectedly complex, yet highly symmetric magnetic structure comprised of non-coplanar, counter-rotating iridium magnetic moments located in zig-zag chains. Remarkably, the magnetic structure exhibits no net ferromagnetic or antiferromagnetic spin correlations, and as such one can rule out a model Hamiltonian whose primary ingredient is the nearest-neighbor Heisenberg interaction. Instead, motivated by the work of Jackeli and Khaliullin [17], and by arguments based on susceptibility anisotropy [13, 15], we present a minimal spin Hamiltonian with dominant Kitaev interactions that naturally reproduces all key features of the observed magnetic order, in particular, we point out that counter rotating spirals on the zig-zag chains are naturally generated by Kitaev interactions. Our results therefore provide strong evidence that dominant Kitaev couplings govern the magnetic interactions in γ -Li₂IrO₃.

The RMXD experiments were performed using the I16 beamline at Diamond (see [18] for details). Systematic searches along high-symmetry directions in reciprocal space revealed that at low temperatures new magnetic Bragg peaks appeared at satellite positions of reciprocal lattice points with an incommensurate propagation vector $\mathbf{q} = (0.57(1), 0, 0)$ [19]. The satellite peaks were found to be as sharp as structural peaks in all three reciprocal space directions, as illustrated for the $(0, 0, 16)+\mathbf{q}$ reflection in Fig. 1a); indicating coherent, 3D magnetic ordering. The peaks disappeared upon heating [Fig. 1(a), open circles] and the temperature-dependence of the intensity had a typical order parameter behavior [see Fig. 1(b)]. The absolute temperature values have been corrected for beam-heating effects through a calibration against specific heat measurements on the *same* sample, shown in Fig. 1(b) inset, which give $T_N = 39.5$ K.

The magnetic origin of the satellite reflections was further confirmed by analyzing the polarization of the scattered beam. Fig. 1(c) shows that the peak at $(0, 0, 16)+\mathbf{q}$

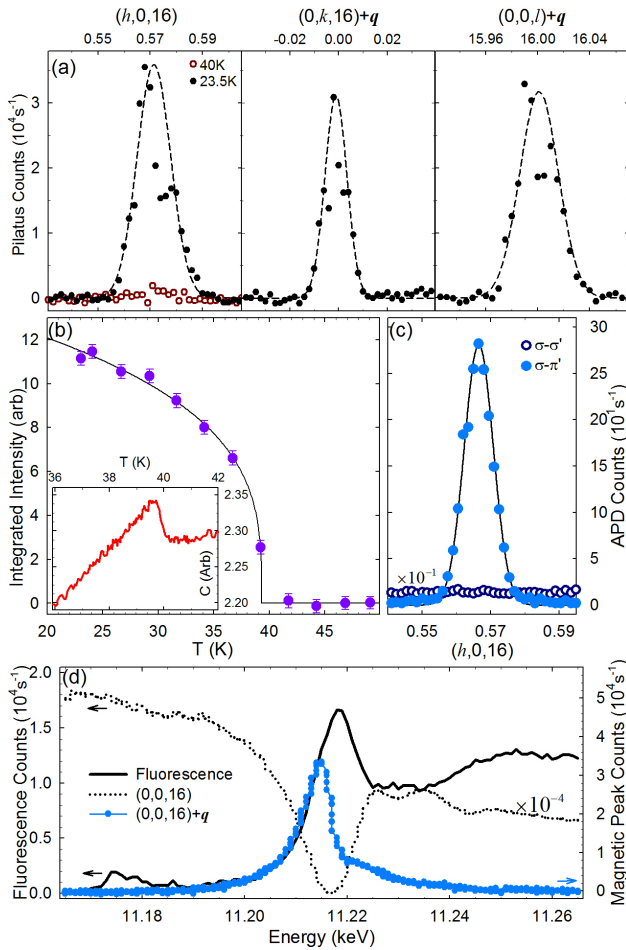


FIG. 1: (color online) Magnetic Bragg peak at $(0, 0, 16) + \mathbf{q}$. (a) Scans along orthogonal directions in reciprocal space (filled/open symbols at base temperature/above T_N). Dashed lines are fits to a Gaussian shape. (b) Temperature-dependence of the integrated magnetic peak intensity (solid line is guide to the eye, temperature values are corrected for beam heating effects, see text). Inset: specific heat data showing an anomaly at the onset of magnetic order. (c) Scans with a polarizer in the scattered beam: the magnetic signal is present only in the $\sigma\text{-}\pi'$ channel (filled circles) and disappears in the $\sigma\text{-}\sigma'$ channel (open circles) dominated by charge scattering (intensity scaled by $1/10$). (d) Energy scan through the magnetic peak (blue squares) and a structural Bragg peak $(0, 0, 16)$ (dotted line, scaled by $1/10^4$), as well as the fluorescence scan (solid line).

appeared only in the $\sigma\text{-}\pi'$ channel (filled circles), and is absent in the $\sigma\text{-}\sigma'$ channel (open circles), as expected for resonant diffraction that is of pure magnetic origin [16]. An energy scan performed whilst centered on the magnetic peak [Fig. 1(d)] showed a large resonant enhancement of the scattered intensity, again as expected for RMXD. The energy dependence is in stark contrast to that characteristic of a nearby structural peak (dotted line). Furthermore, the obtained resonance energy is similar to values found in other iridates [5, 20] and

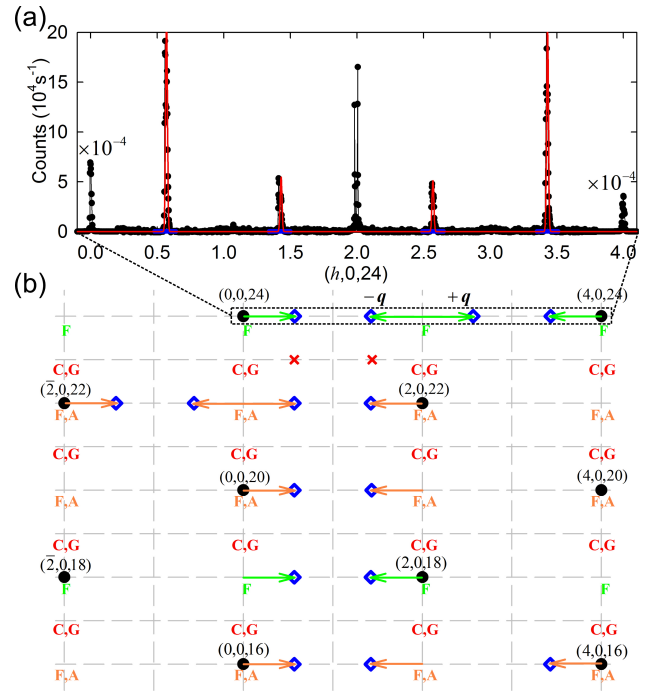


FIG. 2: (color online) (a) Scan along the $(h, 0, 24)$ direction observing structural peaks at $h = 0, 4$ (intensity scaled by $1/10^4$ for clarity), a multiple-scattering signal centered at $h = 2$, and magnetic peaks at $h = 0 + q, 2 \pm q, 4 - q$. Solid red line is the calculated magnetic scattering intensity [21] for the magnetic structure model depicted in Fig. 4. (b) $(h, 0, l)$ reciprocal plane with filled circles, diamonds and red crosses indicating positions of structural peaks, measured magnetic peaks and the absence of peaks, respectively. Lattice points are also labelled by the magnetic basis vectors that have finite structure factor for magnetic peaks at satellite $\pm \mathbf{q}$ positions.

agrees well with the edge of the measured fluorescence signal from the sample (solid line in Fig. 1(d)).

In total over 30 magnetic Bragg peaks were observed, and those measured in the $(h, 0, l)$ -plane are labelled in Fig. 2(b). A representative scan along the $(h, 0, 24)$ direction is plotted in Fig. 2(a), which shows strong structural Bragg peaks centered at $h = 0, 4$, a multiple scattering signal centered at $h = 2$, and four magnetic Bragg peaks symmetrically displaced away from the above reflections. The scan illustrates the highly symmetric nature of the magnetic peak intensities and that \mathbf{q} is distinctly different from the commensurate wavevector $(\frac{1}{2}, 0, 0)$.

The magnetic iridium ions are located on two inequivalent sublattices in the orthorhombic unit cell, referred to as Ir and Ir', respectively (light and dark balls in Fig. 4). Each sublattice contains four sites in the primitive cell labelled 1 to 4 and 1' to 4', respectively. For a propagation vector $\mathbf{q} = (q, 0, 0)$ symmetry analysis [22] gives four types of magnetic basis vectors for each of the two sublattices: $++++(F)$, $++--(C)$, $+--+ (A)$ and $+-+- (G)$ where the \pm signs denote a symmetry-imposed relation between the magnetic Fourier components at the sites 1-

4 and $1'-4'$. There are no symmetry constraints between the basis vectors on the two sublattices.

Each of the four types of basis vectors has its own selection rules for a non-zero structure factor, so their presence can be directly confirmed from the observation of magnetic reflections at certain positions, and in some cases one can also identify the phase relation between the two sublattices. For example, all magnetic peaks along the $(h, 0, 24)$ line in Fig. 2a) can be uniquely assigned to scattering from F -type basis vectors. Satellites at $h = 0 + q$ and $4 - q$ arise from components that are equal in magnitude and in phase on the two sublattices, (F, F) in short-hand notation, whereas the satellites at $h = 2 \pm q$ originate from scattering by components equal in magnitude, but with opposite sign on the two sublattices, i.e. $(F, -F)$ (see [18] for details). The overall selection rules for magnetic scattering are illustrated in Fig. 2b). We have ruled out the presence of both C and G basis vectors as systematic searches (at 4 different azimuth angles) at the satellite positions $(0, 0, 23) + q$ and $(2, 0, 23) - q$ (red crosses) gave no sign of a magnetic signal. Furthermore, the observation of an AG magnetic peak at $(1, 1, 21) - q$, G being ruled out, confirms the presence of an A basis vector (azimuth scan in Fig. 3(a)).

The polarization dependence of the RMXD intensity allows a direct identification of the orientation of the magnetic moments. For a σ -polarized incident beam only the projection of the magnetic moments along the scattered beam direction, \hat{k}' , contribute to the diffraction intensity.[16] By rotating the sample around the scattering vector $\mathbf{Q} = \mathbf{k}' - \mathbf{k}$ by the azimuth angle, Ψ , [see diagram in Fig.3a) inset] the projection of the magnetic moments onto \hat{k}' changes, giving a clear signature of the moment direction. We have measured the azimuth dependence for three magnetic peaks close to the sample surface normal, such that the Ψ rotation is almost around (001). The origin, $\Psi = 0$, is defined as when the (010) direction is in the scattering plane and pointing away from the source. Fig. 3a) shows the azimuth scan for a pure- A magnetic Bragg peak. The intensity drops to zero at $\Psi = 0$ and 180° and has maxima at $\pm 90^\circ$, uniquely identifying that scattering comes from magnetic moment components along x (here x, y, z are along the orthorhombic a, b, c axes and scattering from y - and z -moment components, blue and green lines, respectively, have been calculated for comparison); hence identifying basis vector components in the combination $(A, \pm A)_x$, where the two sublattices are assumed to have equal magnitude moments. Similarly, the azimuth of the pure- F peak in Fig. 3b) originates from y -components antiparallel on the two sublattices, identifying the basis vector $(F, -F)_y$. Fig. 3c) shows the azimuthal dependence for a mixed FA peak, which uniquely identifies it as coming from basis vector components $\pi/2$ out-of-phase in the combination $i(A, -A)_x, (F, F)_z$. We note that this combination of relative phases between the x and z compo-

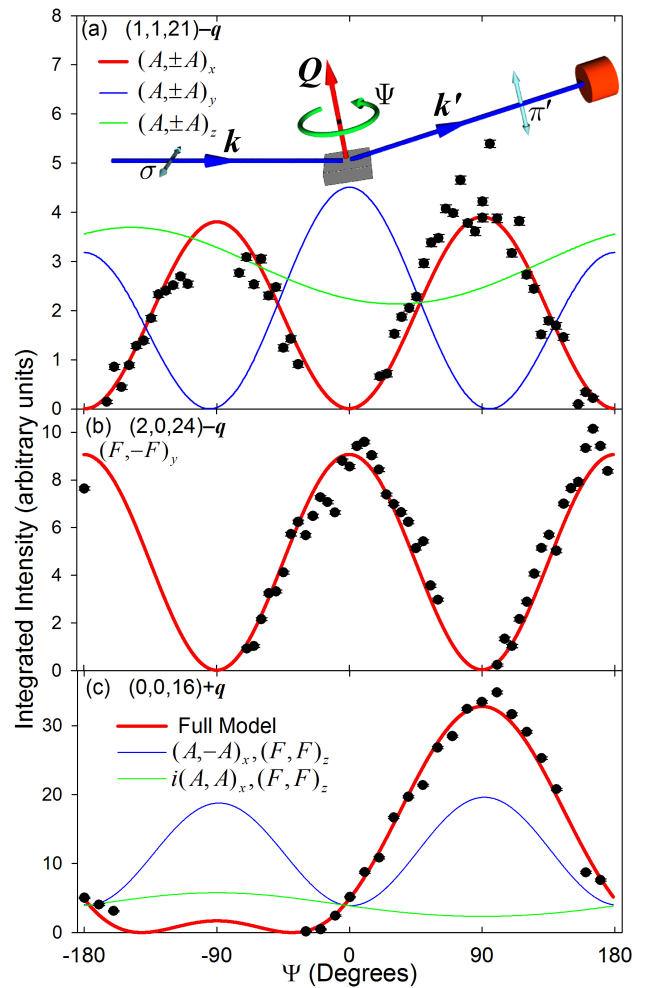


FIG. 3: (color online) Integrated intensity as a function of azimuth for three magnetic Bragg peaks, a) pure- A_x , b) pure- F_y and c) mixed- $F_z A_x$. Top diagram illustrates the scattering geometry. Data points (filled circles) are integrated peak intensities from rocking curve scans corrected for absorption and Lorentz factor. Thick (red) lines show fits that include all contributions to the RMXD structure factor [16, 21] from the magnetic structure model $i(A, -A)_x, -i(F, -F)_y, (F, F)_z$, depicted in Fig. 4. Blue/green curves in a,c) illustrate that other phase combinations of basis vectors are ruled out.

nents on all the iridium sites is unique, where other combinations can be qualitatively ruled out (see blue/green curves in the same figure). The observed phase combination describes counter-rotating moments between consecutive sites along c (curly arrows in Fig. 4), which form counter-rotating zig-zag chains along a .

To determine the relative magnitudes of the magnetic moment components we performed a simultaneous fit to the magnetic scattering intensities in the three azimuth scans in Fig. 3 with four free parameters: the magnitudes of the moment amplitudes M_x and M_y relative to M_z , an overall intensity scale factor for the $(1, 1, 21) - q$ and $(2, 0, 24) - q$ peaks and a separate in-

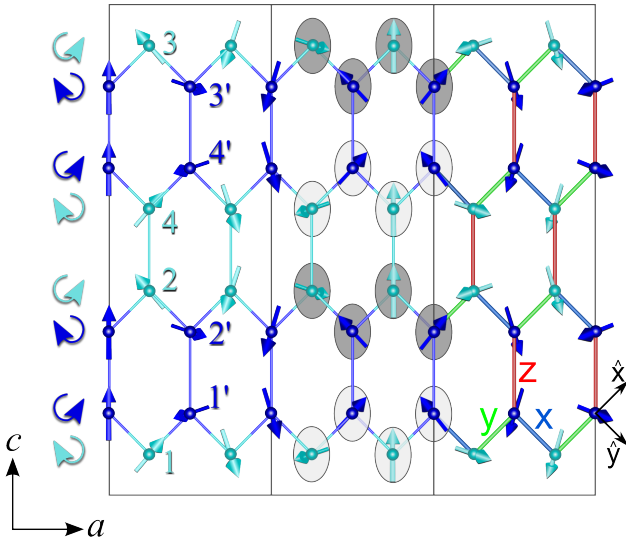


FIG. 4: (color online) Projection of the magnetic structure on the (\mathbf{a}, \mathbf{c}) plane showing 3 unit cells along the horizontal propagation direction \mathbf{a} . Light and dark blue arrows show the moments on the Ir and Ir' sublattices, with sites 1 – 4 and 1' – 4', respectively. Curly arrows on the left side illustrate counter-rotating magnetic order between consecutive sites along \mathbf{c} . In unit cell 2 light ($-\phi$) and dark ($+\phi$) shaded elliptical envelopes emphasize the confinement of the moments to alternate planes obtained from the (ac) plane by a rotation by $\mp\phi$ around \mathbf{c} . In unit cell 3 color of bonds indicates the anisotropy axis of the Kitaev exchanges in (1), with $\eta = x, y, z$ for blue/green/red bonds, where $\hat{\mathbf{x}} = (\hat{\mathbf{a}} + \hat{\mathbf{c}})/\sqrt{2}$, $\hat{\mathbf{y}} = (\hat{\mathbf{a}} - \hat{\mathbf{c}})/\sqrt{2}$ and $\hat{\mathbf{z}} = \hat{\mathbf{b}}$.

tensity scale factor for the $(0, 0, 16)+\mathbf{q}$ peak (which was measured on the same sample, but in a different experiment). The fit is shown by red solid lines in Fig. 3a-c), and gave values for the moment magnitude ratios $M_x : M_y : M_z = 0.65(4) : 0.58(1) : 1$. We note that this also quantitatively reproduces the observed ratio of the magnetic peak intensities in Fig. 2a) (red line).

Imposing the constraint of near-constant magnitude moment at every site requires the phase offset between the x and y components to be π or 0, giving the basis vector combination $i(A, -A)_x, i(-1)^m(F, -F)_y, (F, F)_z$, with $m = 1$ or 2. Both give similar structures and we plot in Fig. 4 the case $m = 1$. The moments are confined to rotate in one of two planes, obtained from the (ac) plane by rotation around the \mathbf{c} -axis by an angle $\pm\phi$, with $\phi = \tan^{-1} \frac{M_y}{M_x} = 42(2)^\circ$. The pattern is such that neighboring iridium zig-zag chains have alternate orientations of the spin rotation plane as indicated by the light and dark shaded envelopes in Fig. 4. The $m = 2$ case simply gives the opposite alternation of the rotation planes.

A key feature of the magnetic structure is the counter-rotation of neighboring moments. On two such sites, say 1 and 1', the spins projected to the ac -plane are $\mathbf{S}_{1,1'}(\mathbf{r}) = \hat{\mathbf{c}}\langle S^c \rangle \cos \mathbf{q} \cdot \mathbf{r} \pm \hat{\mathbf{a}}\langle S^a \rangle \sin \mathbf{q} \cdot \mathbf{r}$. We now rotate from the crystallographic a, b, c -axes to the Kitaev

x, y, z -axes (see Fig. 4 caption) and consider the correlation between the S^x spin components $S_1^x S_{1'}^x$ across an x -type bond, or $S_1^y S_{1'}^y$ across a y -type bond. The net averaged correlation is finite, $\langle S_1^x S_{1'}^x \rangle_x = \langle S_1^y S_{1'}^y \rangle_y = \langle S^a \rangle \langle S^c \rangle \frac{1}{2} \sin \frac{\pi q}{2}$. We see that along each x -type bond the spins are aligned when they point along x , and anti-aligned when they point along y , and similarly for y -type bonds. Thus Kitaev interactions can stabilize the counter-rotating moments with a propagation vector \mathbf{q} along \mathbf{a} . We therefore construct the following Kitaev-Heisenberg Hamiltonian as a minimal model

$$\mathcal{H} = \sum_{c\text{-bonds}} [K_c S_i^{\eta_{ij}} S_j^{\eta_{ij}} + J_c \mathbf{S}_i \cdot \mathbf{S}_j + I_c^c S_i^c S_j^c] + \sum_{d\text{-bonds}} [K_d S_i^{\eta_{ij}} S_j^{\eta_{ij}} + J_d \mathbf{S}_i \cdot \mathbf{S}_j] + \sum_{2^{\text{nd}} \langle\langle ij \rangle\rangle} J_2 \mathbf{S}_i \cdot \mathbf{S}_j \quad (1)$$

where interactions along the vertical (along \mathbf{c}) bonds are denoted by the subscript c and interactions along the zig-zag (diagonal) bonds are denoted by the subscript d . K_c and K_d are the Kitaev interactions along c -bonds (of type $\eta_{ij} = z$) and d -bonds (of type $\eta_{ij} = x$ or y), respectively. To prevent $(0, 0, q_c)$ instabilities we have introduced an Ising coupling I_c^c of the S^c spin components, and finally a Heisenberg coupling J_2 between second nearest neighbors. We take the following values for the parameters (in units of meV): $K_c = -15, K_d = -12, J_c = 5, J_d = 2.5, I_c^c = -4.5, J_2 = -0.9$ [18], where the overall scale was set such as to have the calculated ordering transition temperature agree with the experimental value.

The Hamiltonian was analyzed in Fourier space using the Luttinger-Tisza approximation [18]. This gave the lowest-energy mode identical to the (S^a, S^c) coplanar projection of the magnetic structure in Fig. 4 with $\langle S^c \rangle > \langle S^a \rangle$. To obtain fixed-length spins requires mixing with another mode, and the lowest energy mode available at the same wavevector has collinear order of the S^b components with a pattern such that the mixed mode exactly reproduce the observed non-coplanar structure. Furthermore, the S^b components are co-aligned along all the \mathbf{c} -axis bonds, and hence stabilized by the large FM K_c Kitaev exchange. The mixing amplitude, related to the tilt angle ϕ , is fixed for unit length spins, but changes continuously with the Hamiltonian parameters. Decreasing the strength of the Kitaev interactions prevents the ground state from producing unit-length spins through this mixing mechanism, and importantly, we find that the non-coplanar tilt angle observed in γ -Li₂IrO₃ requires relatively large Kitaev exchanges within the minimal model.

To summarize, through RMXD measurements on γ -Li₂IrO₃ single crystals we have observed an incommensurate, non-coplanar magnetic structure with counter-rotating moments. A Kitaev-Heisenberg Hamiltonian can fully explain the observed complex magnetic structure, providing strong evidence that γ -Li₂IrO₃ is an experimental realization of 3D Kitaev physics in the solid

state.

This work was supported by EPSRC (UK) and by the U.S. Department of Energy, Office of Basic Energy Sciences, Materials Sciences and Engineering Division, under Contract No. DE-AC02-05CH11231.

-
- [1] A. Kitaev, Ann. Phys. (N.Y.) **321**, 2 (2006).
 [2] J. Chaloupka, G. Jackeli and G. Khaliullin, Phys. Rev. Lett. **105**, 027204 (2010).
 [3] B. J. Kim, H. Ohsumi, T. Komesu, S. Sakai, T. Morita, H. Takagi, T. Arima, Science **323**, 1329 (2009).
 [4] Y. Singh, P. Gegenwart, Phys. Rev. B **82**, 064412 (2010).
 [5] X. Liu, T. Berlijn, W.-G. Yin, W. Ku, A. M. Tsvelik, Young-June Kim, H. Gretarsson, Yogesh Singh, P. Gegenwart, and J. P. Hill, Phys. Rev. B **83**, 220403(R) (2011).
 [6] S. K. Choi, R. Coldea, A. N. Kolmogorov, T. Lancaster, I. I. Mazin, S. J. Blundell, P. G. Radaelli, Yogesh Singh, P. Gegenwart, K. R. Choi, S.-W. Cheong, P. J. Baker, C. Stock, and J. Taylor, Phys. Rev. Lett. **108**, 127204 (2012).
 [7] F. Ye, S. Chi, H. Cao, B. C. Chakoumakos, J. A. Fernandez-Baca, R. Custelcean, T. F. Qi, O. B. Korneta, and G. Cao, Phys. Rev. B **85**, 180403(R) (2012).
 [8] H. Gretarsson, J. P. Clancy, Y. Singh, P. Gegenwart, J. P. Hill, J. Kim, M. H. Upton, A. H. Said, D. Casa, T. Gog, and Y.-J. Kim, Phys. Rev. B **87**, 220407(R) (2013).
 [9] M. J. O'Malley, H. Verweij and P.M. Woodward, J. Solid State Chem. **181**, 1803 (2008).
 [10] Y. Singh, S. Manni, J. Reuther, T. Berlijn, R. Thomale, W. Ku, S. Trebst, and P. Gegenwart, Phys. Rev. Lett. **108**, 127203 (2012).
 [11] S. Mandal and N. Surendran, Phys. Rev. B **79**, 024426 (2009).
 [12] Eric Kin-Ho Lee, R. Schaffer, S. Bhattacharjee, and Y. B. Kim, Phys. Rev. B **89**, 045117 (2014).
 [13] I. Kimchi, J. G. Analytis, A. Vishwanath, arXiv:1309.1171 (2013).
 [14] T. Takayama, A. Kato, R. Dinnebier, J. Nuss, H. Takagi, arXiv.org/1403.3296 (2014).
 [15] K. A. Modic, T. E. Smidt, I. Kimchi, N. P. Breznay, A. Biffin, S. Choi, R. D. Johnson, R. Coldea, P. Watkins-Curry, G. T. McCandless, J. Y. Chan, F. Gandara, Z. Islam, A. Vishwanath, A. Shekhter, R. D. McDonald, and J. G. Analytis, Nature Comm **5**, 4203 (2014).
 [16] J. P. Hill, D. F. McMorrow, Acta Cryst A **52**, 236, (1996).
 [17] G. Jackeli and G. Khaliullin, Phys. Rev. Lett. **102**, 017205 (2009).
 [18] Supplemental material
 [19] The uncertainty in the value of q is estimated from combining uncertainties in the crystal orientation (UB-matrix) and the I16 instrument intrinsic sphere of uncertainty.
 [20] S. Boseggia, R. Springell, H. C. Walker, H. M. Rønnow, Ch. Rüegg, H. Okabe, M. Isobe, R. S. Perry, S. P. Collins, and D. F. McMorrow, Phys. Rev. Lett. **110**, 117207 (2013).
 [21] <http://forge.ill.eu/svn/magnetix>
 [22] *Basireps* software part of the *FullProf* suite, J. Rodriguez-Carvajal, Physica B **192**, 55 (1993).

- [23] J. G. Rau, Eric Kin-Ho Lee, H. Y. Kee, Phys. Rev. Lett. **112**, 077204 (2014).

SUPPLEMENTAL MATERIAL

Here we provide additional information on 1) the crystal structure, 2) the magnetic structure, 3) magnetic structure factor calculations, 4) the sample and experimental setup used in the resonant magnetic x-ray diffraction (RMXD) experiments, 5) the RMXD intensity from moment-rotating structures, 6) a description of how Kitaev interactions stabilize counter-rotating moments, and 7) details of the Luttinger-Tisza analysis of the minimal model Hamiltonian.

S1. CRYSTAL STRUCTURE OF γ -Li₂IrO₃

γ -Li₂IrO₃ has an orthorhombic crystal structure depicted in Fig. S1 with edge-sharing IrO₆ octahedra arranged in a three-dimensional network with a three-fold local coordination. The iridium atoms (red balls) form vertically-linked honeycomb rows (light and dark shading) that run alternately along the $\mathbf{a} \pm \mathbf{b}$ diagonals upon moving along the c -axis. For reference the full structural parameters from [15] are listed in Table S1 (A.D.P. are atomic displacement parameters). To simplify the notation for the discussion of the magnetic structure we have labelled the two iridium sublattices as Ir and Ir'.

S2. MAGNETIC STRUCTURE DESCRIBED IN TERMS OF BASIS VECTORS

The magnetic ions are located on the two iridium sublattices, Ir at $8k$ (0.25, 0.25, z), $z = 0.0836(2) \approx 1/12$ and Ir' at $8i$ (0.5, 0.5, z'), $z' = 0.1670(3) \approx 1/6$, each with four sites in the primitive unit cell labelled 1 – 4 and 1' – 4' with coordinates listed explicitly in Table S3 and positions labelled in Fig. S2. For a magnetic structure with propagation vector $\mathbf{q} = (q, 0, 0)$ symmetry analysis [22] gives four types of basis vectors $+++ (F)$, $++-- (C)$, $+-- (A)$ and $+--+ (G)$ for each of the two iridium sublattices, which transform according to the irreducible representations listed in Table S2. The basis vectors encode symmetry-imposed relations between the Fourier components of the magnetic

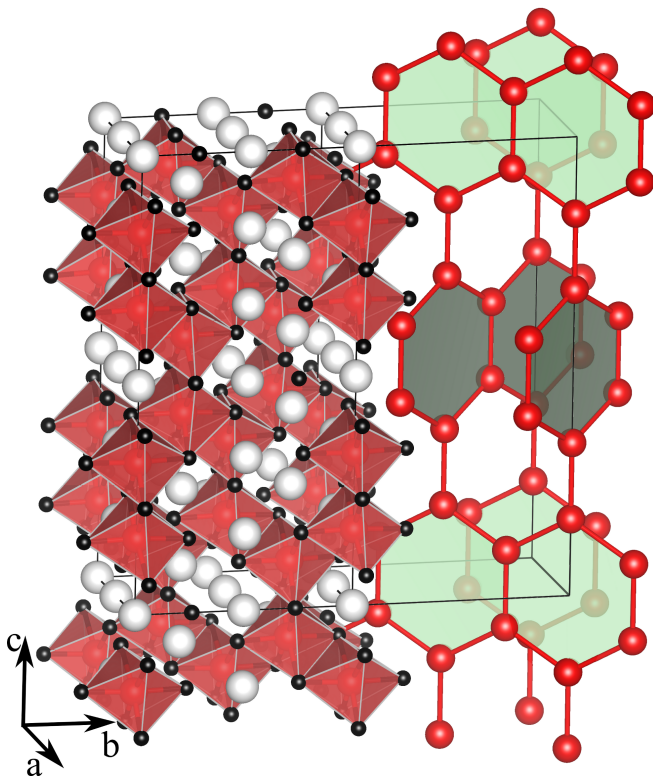


FIG. S1: (color online) Crystal structure of γ -Li₂IrO₃. Two neighbouring unit cells are shown: (left) full structure with Li (white balls), O (black) and Ir (red) located inside IrO₆ octahedra (shaded polyhedra), (right) 3D iridium lattice connectivity: honeycomb rows alternating in orientation (light and dark shading) are interconnected along c .

moments at the different sites, i.e. for basis vector A on the Ir sublattice the Fourier components on sites 1-4 are related by $M_{\pm\mathbf{q},1} = -M_{\pm\mathbf{q},2} = -M_{\pm\mathbf{q},3} = M_{\pm\mathbf{q},4}$. As described in the main text based on diffraction data the basis vectors are found to occur in the combination $i(A, -A)_x, i(-1)^m(F, -F)_y, (F, F)_z$ with moment amplitudes M_x, M_y, M_z , and $m = 1$ or 2 . In both cases the magnetic structure corresponds to a mixture of two irreducible representations Γ_3 (A_x and F_z) and Γ_4 (F_y) in Table S2. The magnetic moment at position \mathbf{r} belonging to a site index $n = 1 - 4, 1' - 4'$ is

$$\mathbf{M}_n(\mathbf{r}) = [\hat{\mathbf{x}}M_x v_x(n) + (-1)^m \hat{\mathbf{y}}M_y v_y(n)] \sin \mathbf{q} \cdot \mathbf{r} + \hat{\mathbf{z}}M_z v_z(n) \cos \mathbf{q} \cdot \mathbf{r} \quad (2)$$

where $\hat{\mathbf{x}}, \hat{\mathbf{y}}, \hat{\mathbf{z}}$ are unit vectors along the orthorhombic $\mathbf{a}, \mathbf{b}, \mathbf{c}$ axes, respectively. $v_{x,y,z}$ are combined (8-site) basis vectors for the two sublattices expressed in shorthand vector notation as $v_x = (A, -A)$, $v_y = (F, -F)$, $v_z = (F, F)$ and with values listed explicitly for all sites in the primitive cell in Table S3. The Fourier components of

TABLE S1: Structural parameters of γ -Li₂IrO₃ at 300 K [15].

Cell parameters					
Space group: $Ccmm$ (#66, origin choice 1)					
$Z = 16$					
$a, b, c(\text{\AA}): 5.9119(3) \ 8.4461(5) \ 17.8363(10)$					
$\alpha, \beta, \gamma(^{\circ}): 90 \quad 90 \quad 90$					
Volume (\AA^3): 890.61(9)					
Fractional atomic coordinates and isotropic A.D.P.'s					
Atom	Site	x	y	z	$U_{\text{iso}}(\text{\AA}^2)$
Ir	$8k$	0.25	0.25	0.0836(2)	0.0124(4)
Ir'	$8i$	0.5	0.5	0.1670(3)	0.0206(6)
Li1	$8j$	0	0.5	0.3333	0.01
Li2	$8k$	0.75	0.25	0.25	0.01
Li3	$8k$	0.75	0.25	0.91667	0.01
Li4	$4c$	0.5	0.5	0.5	0.01
Li5	$4d$	0.5	0	0	0.01
O1	$16m$	0.77(1)	0.515(3)	0.087(4)	0.02(1)
O2	$8g$	0.72(2)	0.5	0.25	0.04(1)
O3	$8l$	0.00(1)	0.262(8)	0	0.006(9)
O4	$16m$	0.49(1)	0.262(6)	0.163(3)	0.006(9)

TABLE S2: Irreducible representations and basis vectors for a magnetic structure with propagation vector $\mathbf{q} = (q, 0, 0)$.

Irreducible representation	Basis vectors
Γ_1	C_x, A_y, G_z
Γ_2	F_x, G_y, A_z
Γ_3	A_x, C_y, F_z
Γ_4	G_x, F_y, C_z

the magnetic moments are

$$\mathbf{M}_{\mathbf{q},n} = i \left[\hat{\mathbf{x}} \frac{M_x}{2} v_x(n) + (-1)^m \hat{\mathbf{y}} \frac{M_y}{2} v_y(n) \right] + \hat{\mathbf{z}} \frac{M_z}{2} v_z(n) \quad (3)$$

with $\mathbf{M}_{-\mathbf{q},n} = \mathbf{M}_{\mathbf{q},n}^*$ as the magnetic moment distribution is real. Eqs. (2,3) describe all iridium sites, including those related by the C -centering translation $(\frac{1}{2}, \frac{1}{2}, 0)$, where \mathbf{r} is the actual position of the ion and n is the site index at the equivalent position $(1 - 4, 1' - 4')$ in the primitive unit cell.

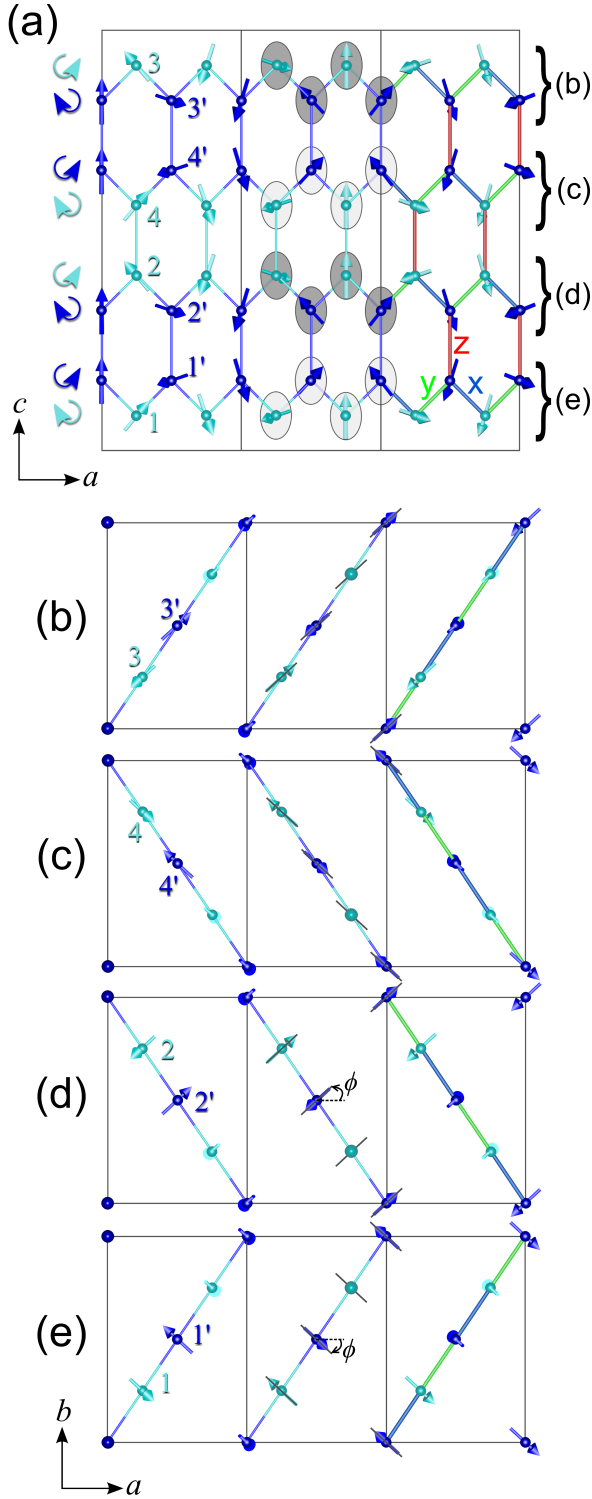


FIG. S2: (color online) (a) Projection of the magnetic structure on the ac plane highlighting counter-rotation of moments between the different sites (1-4, 1'-4') of the primitive cell. Light/dark shading of the elliptical moment envelopes indicate an alternating tilt of the plane of moments' rotation away from the (ac) plane. Right-hand labels (b)-(e) indicate where slices through the magnetic structure are taken at different heights in the unit cell and projected onto the (ab) plane to illustrate the direction of the zig-zag chains. Note the alternating tilt of the plane of rotation of the moments away from the ac plane by $\pm\phi$ between consecutive zig-zag chains stacked along c .

TABLE S3: Fractional atomic coordinates of the iridium sites in the primitive cell and corresponding magnetic basis vector components in the determined magnetic structure.

Site	Coordinates	v_x	v_y	v_z
1	(0.25, 0.25, z)	+	+	+
2	(0.25, 0.75, $0.5 - z$)	-	+	+
3	(0.25, 0.25, $1 - z$)	-	+	+
4	(0.25, 0.75, $0.5 + z$)	+	+	+
1'	(0.5, 0.5, z')	-	-	+
2'	(0.5, 0.5, $0.5 - z'$)	+	-	+
3'	(0.5, 0.5, $1 - z'$)	+	-	+
4'	(0.5, 0.5, $0.5 + z'$)	-	-	+

S3. MAGNETIC STRUCTURE FACTORS

The structure factor for a magnetic Bragg reflection at wavevector $\mathbf{Q} = (h, k, l) \pm \mathbf{q}$ is

$$\mathcal{F}(\mathbf{Q}) = \mathcal{F}((h, k, l) \pm \mathbf{q}) = \sum_n \mathbf{M}_{\pm \mathbf{q}, n} e^{i\mathbf{Q} \cdot \mathbf{r}_n} \quad (4)$$

where the sum extends over all 16 iridium sites in the orthorhombic unit cell (1-4, 1'-4' and their C -translated positions) and $\mathbf{M}_{\pm \mathbf{q}, n}$ are the Fourier components of the magnetic moments at site n with position in the unit cell \mathbf{r}_n . Direct calculation of the structure factors shows that the four types of basis vectors F , C , A and G produce finite intensity magnetic peaks only for satellites of certain integer (h, k, l) reciprocal lattice positions and not others. To make those selection rules transparent we have calculated the structure factors analytically for an "ideal" iridium lattice, which is very close to the one refined experimentally in Table S1, but with the Ir coordinate at $z = 1/12$ and Ir' at $z' = 1/6$. In this case the structure factors are obtained as:

$$\mathcal{F}_F(\mathbf{Q}) = 8e^{i\zeta_{\pm}} \mathbf{M}_{\pm \mathbf{q}, 1} \cos \frac{\pi l}{6} \left[\cos \frac{\pi(k+l)}{2} + e^{\pm i\alpha} e^{i\frac{\pi(h+l)}{2}} \cos \frac{\pi l}{2} \right] \delta_{h+k, 2p} \quad (5)$$

$$\mathcal{F}_C(\mathbf{Q}) = 8e^{i\zeta_{\pm}} \mathbf{M}_{\pm \mathbf{q}, 1} \left[\sin \frac{\pi l}{6} \sin \frac{\pi(k+l)}{2} - i e^{\pm i\alpha} e^{i\frac{\pi(h+l)}{2}} \cos \frac{\pi l}{6} \sin \frac{\pi l}{2} \right] \delta_{h+k, 2p} \quad (6)$$

$$\mathcal{F}_A(\mathbf{Q}) = 8i e^{i\zeta_{\pm}} \mathbf{M}_{\pm \mathbf{q}, 1} \sin \frac{\pi l}{6} \left[\cos \frac{\pi(k+l)}{2} - e^{\pm i\alpha} e^{i\frac{\pi(h+l)}{2}} \cos \frac{\pi l}{2} \right] \delta_{h+k, 2p} \quad (7)$$

$$\mathcal{F}_G(\mathbf{Q}) = -8e^{i\zeta_{\pm}} \mathbf{M}_{\pm\mathbf{q},1} \left[i \cos \frac{\pi l}{6} \sin \frac{\pi(k+l)}{2} + e^{\pm i\alpha} e^{i\frac{\pi(h+l)}{2}} \sin \frac{\pi l}{6} \sin \frac{\pi l}{2} \right] \delta_{h+k,2p} \quad (8)$$

where δ is the Kronecker symbol and p is an integer, i.e.

$$\delta_{h+k,2p} = \begin{cases} 1, & h+k \text{ even} \\ 0, & h+k \text{ odd} \end{cases}$$

and this term arises in the structure factor due to the C -centering. Here $\zeta_{\pm} = \pi(h/2 \pm q/2 + k + l/3)$ and the 1st and 2nd terms in the square brackets come from the Ir and Ir' sublattices, respectively, where we have assumed that their magnetic Fourier components are the same up to a complex phase offset α , i.e. $\mathbf{M}_{\mathbf{q},1'} = e^{i\alpha} \mathbf{M}_{\mathbf{q},1}$. In the determined magnetic structure the phase offset for the A_x and F_y basis vectors is $\alpha = \pi$, whereas for the F_z basis vector it is $\alpha = 0$.

From the above equations it is clear that in the $(h0l)$ plane, for $l = 6n$ (n integer) only F -basis vectors contribute as the structure factor for all the other basis vectors cancels ($\mathcal{F}_C = \mathcal{F}_A = \mathcal{F}_G = 0$). In this case further inspection of the structure factors shows that satellites can be separated into those corresponding to $\alpha = 0$ and those with $\alpha = \pi$, for example the magnetic satellites at $(0, 0, 24) \pm \mathbf{q}$ come from an (F, F) basis vector ($\alpha = 0$) and peaks at $(2, 0, 24) \pm \mathbf{q}$ come from an $(F, -F)$ basis vector ($\alpha = \pi$). For the $(h, 0, l)$ plane depicted in Fig. 2b) magnetic satellite peaks occur only for h even with the further selection rule l odd for both C and G , and l even for both F , A with pure F (no A contribution) for $l = 6n$, n integer. Satellites of (odd, odd, $l = 3 + 6n$), n integer such as $(1, 1, 21)$ are of A , G type (no F or C contribution) and this is used to prove the existence of an A -basis vector in the magnetic ground state.

S4. RESONANT MAGNETIC X-RAY DIFFRACTION EXPERIMENTS

The sample used in the x-ray experiments was a single crystal of γ -Li₂IrO₃ with a typical rhombic morphology [15] of volume $\sim 35 \times 10^3 \mu\text{m}^3$. The sample quality was checked using a Mo-source SuperNova x-ray diffractometer confirming the previously deduced crystal structure (orthorhombic space group $Cccm$ with lattice parameters $a = 5.9119 \text{ \AA}$, $b = 8.4461 \text{ \AA}$, $c = 17.8363 \text{ \AA}$ at room temperature). Specific heat measurements on this crystal using an in-house ac micro-calorimeter observed a clear anomaly near $T_N = 39.5 \text{ K}$ [see Fig. 1b) inset], in good agreement with the transition temperature to magnetic order inferred from earlier magnetic susceptibility and torque measurements [15].

Resonant x-ray diffraction at the Ir L3 edge (11.215 keV) was performed using the I16 beamline at Diamond in reflection geometry with the crystal mounted with the (001) axis surface normal. The σ -polarized incident beam was de-focused to an area $200 \times 200 \mu\text{m}^2$, to ensure illumination of the entire sample. For the polarization analysis measurements a Au (3, 3, 3) crystal was placed in the scattered beam and intensities were counted in an APD detector, for the rest of the measurements an area detector (Pilatus) was used. The sample was cooled using a closed-cycle refrigerator (CCR) with Be windows with a base temperature of 9 K.

S5. INTENSITY IN RESONANT MAGNETIC X-RAY DIFFRACTION

In the dipolar approximation the magnetic resonant x-ray scattering intensity is proportional to

$$L(\theta) \mathcal{A} \left| (\hat{\epsilon}' \times \hat{\epsilon}) \cdot \mathcal{F}(\mathbf{Q}) \right|^2$$

where $L(\theta)$ is the Lorentz factor at the scattering angle 2θ , \mathcal{A} is an absorption correction dependent upon the experimental geometry, $\mathcal{F}(\mathbf{Q})$ is the magnetic structure factor given in eq. (4), and $\hat{\epsilon}'$ and $\hat{\epsilon}$ are unit vectors along the polarization of the electric field component of the scattered and incident x-ray beams, respectively [16]. For a σ -polarized incident beam magnetic resonant scattering occurs only in the σ - π' channel [see diagram in Fig. 3a) inset], meaning that the product of the electric field polarization vectors is along the scattered beam direction, i.e. $\hat{\epsilon}' \times \hat{\epsilon} = \hat{k}'$.

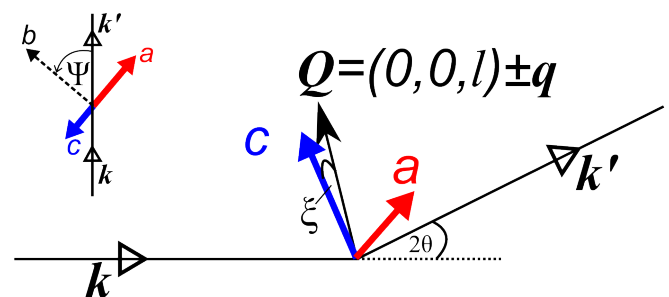


FIG. S3: (color online) Schematic of the x-ray scattering experiment probing the magnetic scattering at $\mathbf{Q} = (0, 0, l) \pm \mathbf{q}$ showing the orientation of the orthorhombic crystal axes at a general azimuth angle Ψ (inset shows projection in the plane normal to \mathbf{Q} indicating the azimuth angle origin). In the main diagram ξ is the angle between \mathbf{Q} and the c -axis, i.e. $\xi = \cos^{-1}(\hat{\mathbf{Q}} \cdot \hat{\mathbf{c}})$.

The orientation of the magnetic moments can be experimentally determined by exploiting the polarization dependence of the scattering intensity as only the component of the structure factor vector along the scattered beam direction, $\mathcal{F}_{\parallel} = \mathcal{F} \cdot \hat{k}'$, contributes. By keeping

the instrument in the scattering condition and rotating the sample around the scattering wavevector $\mathbf{Q} = \mathbf{k}' - \mathbf{k}$ the projection \mathcal{F}_{\parallel} of the structure factor vector varies depending on the azimuth angle Ψ with maximum intensity when the moments that give rise to the scattering make the smallest angle with \mathbf{k}' and zero intensity when they are perpendicular. This is illustrated by the calculated azimuth dependence of the intensity for moments along x , y and z for an A -type basis vector in Fig. 3a) (red, blue, green curves), and the data uniquely identifies that scattering comes from a basis vector with collinear magnetic moments along x .

For magnetic Bragg reflections where moments along two orthogonal directions contribute, such as $(0, 0, 16) + \mathbf{q}$ in Fig. 3c) of mixed A_x , F_z character, the scattering intensity has a cross term that is sensitive to the complex phase between the structure factor vectors along the two directions, so it can distinguish between moments varying sinusoidally along a line in the xz plane (phase offset 0 or π) or rotating in the xz plane (phase offset $\pm\pi/2$). Explicitly, the parallel component of the structure factor when both x and z moments contribute is

$$\mathcal{F}_{\parallel}(\Psi) = \mathcal{F}_z(\cos \xi \sin \theta - \sin \xi \cos \theta \sin \Psi) + \mathcal{F}_x(\sin \xi \sin \theta + \cos \xi \cos \theta \sin \Psi)$$

where $\mathcal{F}_{x,z}$ are the separate structure factors for the magnetic moment components along the x, z -axes and the angles 2θ and ξ are defined in the scattering diagram in Fig. S3. From this the azimuth dependence of the magnetic scattering intensity is obtained as

$$|\mathcal{F}_{\parallel}(\Psi)|^2 = |\mathcal{F}_z|^2(\cos \xi \sin \theta - \sin \xi \cos \theta \sin \Psi)^2 + |\mathcal{F}_x|^2(\sin \xi \sin \theta + \cos \xi \cos \theta \sin \Psi)^2 + \text{Re}(\mathcal{F}_z \mathcal{F}_x^*) [\sin 2\xi (\sin^2 \theta - \cos^2 \theta \sin^2 \Psi) + \sin 2\theta \cos 2\xi \sin \Psi] \quad (9)$$

where $\text{Re}()$ means the real part. The first two terms give the sum of the scattering intensities separately from moments along the two directions, whereas the last term is the cross term. For the specific case of $\mathbf{Q} = (0, 0, l=16) + \mathbf{q}$, the cross term pre-factor is

$$\text{Re}(\mathcal{F}_z \mathcal{F}_x^*) \propto \begin{cases} \mp \cos \frac{\pi l}{6} \sin \frac{\pi l}{6}, & \pm i(A, -A)_x, (F, F)_z \\ 0, & \pm(A, -A)_x, (F, F)_z \end{cases}$$

where \mathcal{F}_x and \mathcal{F}_z are of the form $\mathcal{F}_{(A,-A)}$ and $\mathcal{F}_{(F,F)}$, respectively, from eqs. (5,7). There is no cross-term if moments are in-phase or π out-of-phase and a finite cross-term if moments are $\pm\pi/2$ out-of-phase. The azimuth data in Fig. 3c) clearly shows a large asymmetry around $\Psi = 0$, which is quantitatively explained (red line) by the basis vector combination $i(A, -A)_x, (F, F)_z$ with moments rotating in the xz plane and rules out in-phase or π out-of-phase moments along the x and z axes (blue line).

S6. MAGNETIC STRUCTURE WITH COUNTER-ROTATING MOMENTS STABILIZED BY KITAEV INTERACTIONS

In this section we give details of the derivation of the net spin correlation between nearest-neighbor sites along the d -bonds $\langle S_n^\eta S_{n'}^\eta \rangle_\eta = \langle S^a \rangle \langle S^c \rangle \frac{1}{2} \sin \frac{\pi q}{2}$ with $\eta = x$ or y . First we recall the transformation from the crystallographic axes $\hat{\mathbf{a}}, \hat{\mathbf{b}}, \hat{\mathbf{c}}$ to the Kitaev axes defined as $\hat{\mathbf{x}} = (\hat{\mathbf{a}} + \hat{\mathbf{c}})/\sqrt{2}$, $\hat{\mathbf{y}} = (\hat{\mathbf{a}} - \hat{\mathbf{c}})/\sqrt{2}$ and $\hat{\mathbf{z}} = \hat{\mathbf{b}}$, see Fig. 4.

The a -component of the displacement between adjacent sites of type 1 and 1' in a zig-zag chain is $(\mathbf{r}_1 - \mathbf{r}_{1'}) \cdot \hat{\mathbf{a}} = \pm a/4$, where the upper (lower) sign is to be taken if the two sites are connected by a Kitaev bond of type x (y). More generally, for neighboring sites of type n and n' the displacement projection is $(\mathbf{r}_n - \mathbf{r}_{n'}) \cdot \hat{\mathbf{a}} = \pm \nu_n a/4$, where $\nu_n = +1$ for $n = 1, 4$ and $\nu_n = -1$ for $n = 2, 3$.

In this notation, we obtain from (2) that sites in the rotating magnetic structure carry the spin moment

$$\mathbf{S}_{n,n'}(\mathbf{r}) = \pm \left[\nu_n \hat{\mathbf{a}} \langle S^a \rangle + (-1)^m \hat{\mathbf{b}} \langle S^b \rangle \right] \sin \mathbf{q} \cdot \mathbf{r} + \hat{\mathbf{c}} \langle S^c \rangle \cos \mathbf{q} \cdot \mathbf{r} \quad (10)$$

where the \pm sign in front of the square bracket corresponds to unprimed/primed sites and the case $m = 1$ is depicted in Fig. S2. The product of this \pm sign in front of the square brackets and the ν_n sign factor gives a sign which alternates between $+$ and $-$ when sites are listed by their c -coordinate, i.e. the vertical axis in Fig. 4, producing the counter-rotation of the spin moments in the ac plane.

It is immediately evident that along Kitaev z -type bonds (linking sites of type 1'2', 3'4', 13 and 24, see Fig. S2a)) the $S^z = S^b$ spin components are always ferromagnetically-correlated, enabling energetic stabilization through the strong FM Kitaev interaction on these bonds, $K_c < 0$. The more subtle correlations, as discussed in the main text, are those of the $S^x(S^y)$ spin components across x -type (y -type) Kitaev bonds. The counter-rotation of neighboring moments within the unit cell enables these subtle Kitaev correlations, as follows

$$\begin{aligned} \langle S_n^\eta S_{n'}^\eta \rangle_{\mathbf{r}: \eta\text{-bond}} / \langle S^a \rangle \langle S^c \rangle &= \\ \left\langle \cos \left(\mathbf{q} \cdot \mathbf{r} \pm \nu_n \frac{\mathbf{q} \cdot \mathbf{a} - \pi}{4} \right) \cos \left(\mathbf{q} \cdot \mathbf{r} \pm \nu_n \frac{\pi}{4} \right) \right\rangle_{\mathbf{r}} &= \\ \frac{1}{2} \cos \left(\frac{\mathbf{q} \cdot \mathbf{a} - 2\pi}{4} \right) &= \frac{1}{2} \sin \left(\frac{\mathbf{q} \cdot \mathbf{a}}{4} \right) \end{aligned} \quad (11)$$

with $\eta = x$ or y and $\langle \dots \rangle_{\mathbf{r}}$ indicates the average over all positions \mathbf{r} of sites of type n in the crystal. Note that defining the rotating magnetic structure within the primitive unit cell (containing 8 sites) is sufficient to uniquely specify the spin moments on all sites in the crystallographic a, b, c unit cell, which contains 16 iridium sites; here $\mathbf{q} \cdot \mathbf{a}$ ranges from -2π to 2π . Within our convention of the spin components within the unit cell, positive

values of q (i.e. $0 < \mathbf{q} \cdot \mathbf{a} < 2\pi$) correspond to positive Kitaev correlations, which may be stabilized by FM Kitaev interactions ($K_d < 0$).

S7. LUTTINGER-TISZA ANALYSIS OF THE MINIMAL MODEL HAMILTONIAN

We diagonalize the spin Hamiltonian in momentum space without the unit length constraint. The energies and modes are found as the eigenstates of the 24×24 matrix, corresponding to three spin components for each site in the primitive unit cell. Then solutions obeying the unit length constraint are constructed from the lowest eigenmode, possibly with higher energy modes mixed in.

The lowest eigenvalue of the Hamiltonian in eqn. (1) with parameters as given in the main text occurs at a wavevector numerically indistinguishable from $(4/7, 0, 0)$ (in r.l.u.'s of the orthorhombic unit cell $a \times b \times c$). This minimal energy eigenmode, with energy -13.6 meV, has the ordered spin moment $\mathbf{S} \propto \hat{c} \pm i0.85\nu_n \hat{a}$, with the upper (lower) sign for the unprimed (primed) sites, and hence does not quite obey the constraint of normalized spins. However it does exactly describe the coplanar projection of the experimental magnetic structure onto the

ac plane. The next three eigenmodes again involve only S^a, S^c spin components, and cannot mix with the lowest mode. The fifth eigenmode at this wavevector, with energy -10.5 meV, has spins purely along \hat{b} , with an order pattern of \pm signs for unprimed/primed sites, exactly capturing the pattern of the non-coplanar tilts in the experimentally-determined structure. So mixing between this eigenmode and the lowest energy eigenmode to ensure the constraint of fixed-length spins can match all features of the experimentally-determined magnetic structure. For completeness we note that changing the sign of the mixing coefficient corresponds to changing between the cases $m = 1$ and 2 in eq. (10), with the two structures being degenerate in energy.

In summary, through extensive searches in parameter space for candidate spin Hamiltonians we have found that all couplings in eqn. (1) are required to stabilize the observed magnetic structure as the lowest-energy structure with fixed-length spin moments. The phase obtained is stable within a range of values for the Hamiltonian parameters and the quoted values in the text are a representative solution, where the overall scale is set by the constraint that the calculated transition temperature to magnetic order matches the experimental value.